Kovove Mater. 63 2025 93–106
DOI: 10.31577/km.2025.2.93

Influence of crystallization roller substrate processing method on the failure form of surface WC-Cr_3C_2-Ni coating

Diyao Zhang[1], Sheng Qu[2]*, Zijun Peng[1], Zhenli Liu[1], Jingkun Yu[1], Lei Yuan[1,3]**

[1] *Key Laboratory for Ecological Metallurgy of Multimetallic Mineral (Ministry of Education), Northeastern University, Shenyang 110819, P. R. China*
[2] *Shenyang University of Technology, Mechanical Engineering School, Shenyang 110870, P. R. China*
[3] *Engineering Research Center of Frontier Technologies for Low-Carbon Steelmaking (Ministry of Education), Shenyang 110819, Liaoning, P. R. China*

Received 24 October 2024, received in revised form 12 March 2025, accepted 10 April 2025

Abstract

The changes in physical properties of the crystallization roller prepared by different processing methods, as well as the stability of the WC-Cr_3C_2-Ni coating on it, were investigated in this study. The physical properties of the roller body treated by self-aging were the same as those of standard industrial treatment. The roller hardness reached more than 430.26 HV0.5, the thermal conductivity exceeded 105 $W\,m^{-1}\,K^{-1}$ and exhibited good wear resistance. The rollers of different processing methods showed excellent bearing capacity for coatings. In the extreme service environment, the failure form of the coating on the roller surface was affected by the substrate hardness. When the hardness of the roller increased from 220.72 to 430.26 HV0.5, the failure cracks between the coating and substrate were close to the interface joint. The experimental results showed that both the non-industry standard aged treatment and the standard aged treatment can improve the performance of the roller body at this stage. The thermal shock life of the roller body was increased by 5.3 and 15.8 %, respectively, and the wear volume of the roller body was reduced from 7.05×10^{-3} to 5.23×10^{-3} cm^3 and 5.02×10^{-3} cm^3, respectively. At this time, the overall cost increase of the production line simulation budget was only 0.4 %, which was far lower than the 14.1 % of the roller that was completely replaced. This research effectively reduces the cost of innovation in the actual production of steel mills and provides theoretical support for other HVAF coating applications.

Key words: HVAF spraying, crystallization roller, WC-Cr_3C_2-Ni coating, processing method, economic benefit

1. Introduction

Steel manufacturing capacity had always been an important consideration in measuring the economic strength of a country [1–3]. The continuous casting process has been widely used as a new technology. The crystallizer in the continuous casting machine rapidly cools the molten steel to form a billet [4–6]. To improve the cooling capacity of the crystallizer, the material is generally selected as CuCrZr [7]. The cooling water inside the crystallizer takes away the heat of the liquid steel in the flow process, and such cooling conditions also make the cooling rate of the liquid steel more than 1000 ℃ s^{-1} [8]. In the traditional continuous casting machine, the slab crystallizer is used, and the oscillation of the crystallizer promotes the billet to release from the outlet. With the development of technology and the proposal of an environment-friendly green metallurgy policy, more advanced two-roll thin strip continuous casting technology has been developed. As a near-final technology, the new structural crystallization roller integrates the functions of the crystallizer and the roller [9, 10]. The material of the crystallization roller must have the characteristics of high thermal conductivity and hardness, so the beryllium copper enters the field of vision of researchers.

Beryllium copper, also known as beryllium bronze, is a copper alloy with good mechanical properties and

---

*Corresponding author: e-mail address: qusheng92@163.com
**Corresponding author: e-mail address: yuanl@smm.neu.edu.cn

thermal conductivity [11]. After quenching treatment, beryllium copper has a hardness comparable to steel (more than 200 HV0.5) and is also called semi-hard beryllium copper [12, 13]. At the beginning of the 21st century, domestic iron and steel enterprises explored the possibility of using semi-hard beryllium copper as a new type of crystallization roller material. After applying semi-hard beryllium copper, the production line ran stably, and the annual output of millimeter-grade ultra-thin plate exceeded 500,000 tons. To improve the service life of the crystallization roller, a cermet coating with a wear-resistant protection function is usually deposited on the surface via HVAF technology [14–16]. With the increase in service time, the crystallization roller faces the risk of failure in harsh environments, and further improvement of the performance of the crystallization roller substrate is put on the agenda. It is found that when the semi-hard beryllium bronze undergoes the aging treatment at 320 ℃, the internal structure changes from dendrite to an equiaxial crystal structure, and the thermal conductivity and hardness are improved again. At this time, it is also known as full-hard beryllium bronze. Under the actual working conditions, whether to directly replace the new material roller body or to carry out secondary treatment for the existing roller body has become an important problem to be solved.

The research on the surface coating properties of structural parts mainly focuses on improving coating materials and optimizing preparation technology [17–20]. Even for the heat treatment after the coating preparation, the focus was only on the performance of the coating itself [21]. To our knowledge, few studies have concerned whether the processing method of the substrate influences the preparation of its surface coating, and no studies have mentioned the exact relationship between the failure mode of the component and the change of the substrate structure. When guiding actual large-scale production, researchers should also consider the cost of the whole process, not just limited to small-scale laboratory experiments. In this study, we put forward the scheme of self-secondary heat treatment for the whole crystallization roller. This scheme can not only improve the performance of the WC-Cr_3C_2-Ni coating on the surface of the roller body, but also greatly improve the wear resistance of the roller in the face of coating failure. More importantly, the scheme greatly reduced the cost of consumption compared with replacing new materials and has great potential in industrial technology innovation.

In this study, WC-Cr_3C_2-Ni coating was deposited on the surface of crystallization rollers prepared by different process standards via HVAF technology. The influence of the combination of substrate and coating in different states was investigated. The improvement effect of the substrate processing sequence and standard on the thermal shock resistance of the coating was studied by thermal shock test, and a high-temperature wear test verified the stability of the substrate under the condition of coating failure. The influence of substrate processing technology changes on production line cost was described.

2. Materials and methods

2.1. Experimental materials and coating deposition process

Commercial WC-Cr_3C_2-Ni powders (size: 5–30 μm, 73%WC-20%Cr_3C_2-7%Ni (wt.%), purity: 99.9 %, Zhangyuan Tungsten Industry, P. R. China) were selected as the raw materials for the coatings. Semi-hard and full-hard beryllium bronze C17200 substrates (Cu1.91%Be (wt.%), 20 and 40-mm-diameter bars, Shengzun Material, P. R. China) were used to simulate the crystallization roller in actual production processes. The copper bar underwent a rough and fine polishing on the lathe before being mirror-polished. The surface roughness of the copper bar eventually reached 0.4 μm [22]. Before spraying, the bar's surface was sandblasted by corundum particles. The WC-Cr_3C_2-Ni coatings were deposited using an HVAF system (AucKoteC-01, Kermetico, USA). The main parameters were as follows: air pressure: 0.48 MPa; propane pressure: 0.50 MPa; chamber pressure: 0.43 MPa; hydrogen flow: 0.30 $L\,s^{-1}$; nitrogen flow: 0.38 $L\,s^{-1}$; rotation speed of the powder feeder: 0.73 $rad\,s^{-1}$; powder feed rate: 120 $g\,min^{-1}$; gun transverse speed: 0.02 $m\,s^{-1}$; gun angle: 90°; stand-off distance: 180 mm; spot interval: 3 mm.

2.2. Aging treatment

A vacuum muffle furnace (OTF-1200X, Kejing, P. R. China) was used to heat the sample. The heating temperature of the sample under a vacuum environment was 320 ℃, and the heating time was 2.5 h. Argon was used to clean the furnace's interior twice before aging treatment to eliminate the effect of oxidation on the sample surface. The heating rate was 10 ℃ min^{-1}, and the sample was cooled with the furnace.

2.3. Particle size distribution, hardness, and thermal conductivity measurements

A laser particle size analyzer (Mastersizer 3000, Malvern Panalytical, UK) was used to determine the particle size distribution of the powder materials. A hardness tester (ZD-HVZHT-10, Zongde, P. R. China) was used to test the hardness changes of the coatings and the substrates. In the Vickers hardness test, the

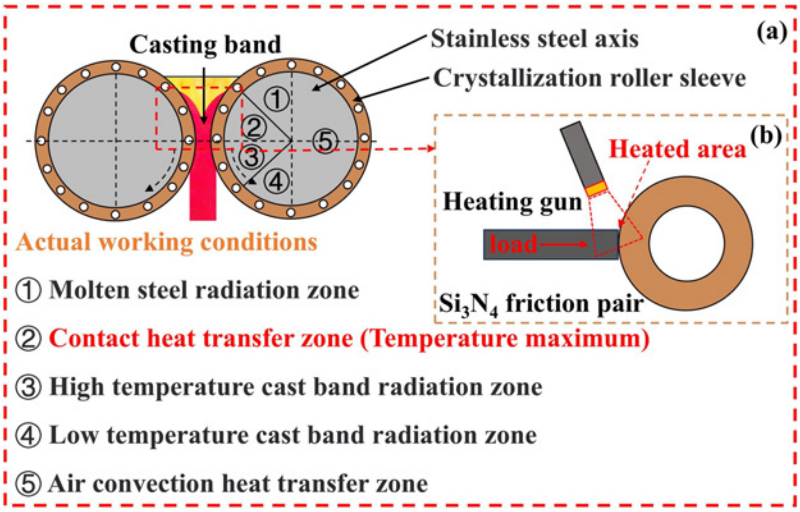

Fig. 1. (a) Crystallization roller service environment, (b) wear tester structure, (c) size of the grinding block sample, and (d) size of the wear ring sample.

samples were subjected to a load of 4.91 N, and the dwell time was 10 s. The same test environment was measured five times, and the average value was taken. A laser thermal conductivity meter (LFA-427, NETZSCH, Germany) was used to test the thermal conductivity of each sample at room temperature (25 ℃). The laser voltage was 450 V, the pulse width was 0.5 ms, and the Ar gas flow rate was 4.17 mL s^{-1}.

2.4. Thermal shock cycles

A high-temperature heat shock furnace (SGM9812A, SGM, P. R. China) was used to test the thermal shock resistance of the coating samples. In each thermal shock cycle, the specimens were first placed in the furnace at 800 ℃ and held for 20 min; they were then removed and placed in water at 25 ℃ for 5 min until completely cooled. The experiments ended when the coatings were detached beyond the centerline of the samples.

2.5. Wear tests of the roller surface covered by the HVAF-sprayed coatings

As shown in Fig. 1a, there is a heat condition of the crystallization roller coating in the actual continuous casting process. A wear tester (MMS-2A, Hengxu, P. R. China) as shown in Fig. 1b is used to simulate the friction and wear of the actual crystallization roller at 200 ℃. As shown in Fig. 1c, it is the size and processing standard of the ring specimen and the counter grinding block specimen in the block-on-ring wear test. In this experiment, a block of Si_3N_4 with a length, width, and height of 6, 7, and 30 mm was used for grinding material, and the hardness reached 1482.62 HV0.5. The surface roughness, parallelism, and perpendicularity of the ring and block specimens were 10 μm. The surface of the coated specimen did not need to be polished before the experiment. The experiment was performed with a load of 50 N at a rotation speed of 20.94 rad s^{-1} for 60 min. To simulate the distribution of the temperature field when the crystallization roller rotates, a spray gun induced local heating in the high-temperature wear experiments. To ensure the accuracy and repeatability of the detection, the experiment was repeated three times.

2.6. Microstructure observation and phase analysis

A metallographic microscope (DSX510, OLYMPUS, Japan) was used to observe the microstructure of the C17200 substrate after erosion. Field-emission scanning electron microscopy (FE-SEM, Su8010, HITACHI, Japan) combined with energy-dispersive spectroscopy (EDS) was used to observe the feedstock powder morphology and the microstructure of the coatings and the substrate after the thermal shock tests and wear tests. The Image Pro Plus software was used to measure the porosity of the coatings. Five regions were randomly selected inside the coating to ensure accurate results. The test image was taken from the coating section image after 3000 times magnification. The phase composition of the feedstock powder and the products generated during the thermal shock tests was analyzed using X-ray diffraction (XRD, Smart Lab 9KW, Rigaku, Japan) with a Cu target at 45 kV and 200 mA (2θ scanning range: 5°–90°, scanning speed: 10° min^{-1}, scan step: 0.01°). The cathode material of the X-ray diffractometer is tungsten wire, and the anode material is the copper target. The X-ray diffractometer used in this experiment was Cu-Kα radiation.

3. Results and discussion

3.1. Microstructure and phase analysis of coatings

In the spraying process, the powder material is heated to molten in the combustion chamber [23]. The powder droplets are bombarded by high-pressure gas, cooled, and solidified on the surface of the substrate to form a coating [24]. To ensure a dense and uniform coating, thermal spray powder materials are usually prepared using the sintering method and crushed using the ball milling method. As shown in Fig. 2a, Cr_3C_2 and Ni phase wrap the WC hard phase and uniform spherical particles. The average size (Dv_{50}) of the powder particle is 18.4 µm, and the production practice has also proved that the coating performance exhibits the best when the powder particle size is between 5–30 µm [25]. As shown in Figs. 2b,c, the WC-Cr_3C_2-Ni powders do not undergo oxidation and decarbonization during sintering and spraying, and the internal components are stable.

Continuous casting is a very mature industrial field that faces great challenges for large-scale innovation, which has led to few studies on crystallization rollers. The main material of crystallization rollers is semi-hard beryllium bronze C17200 (subsequently referred to as semi-hard C17200). As shown in Fig. 3a, the standard semi-hard beryllium bronze exhibits a dendrite structure inside, and the hardness reaches 220.72 HV0.5. At this time, heat treatment was needed to improve the performance of the C17200 further. As shown in Fig. 3b, after aging treatment at 320℃ for 2.5 hours, the internal dendrite structure of semi-hard C17200 is redissolved into the equiaxial crystal structure, and the substrate at this time is also called full-hard C17200 (hardness reaches 430.26 HV0.5) [26]. As shown in Figs. 3c,d, the internal structure of the roller body changes significantly after non-standard aging treatment (handled by oneself). At this time, the grain size of the full-hard C17200 was 21.32 µm, but the structure transformation was not uniform, and the grain boundary was coarse. As shown in Fig. 3e, the grain size of the commercial full-hard C17200 (hardness reaches 426.51 HV0.5) prepared by the industrial standard process is 23.17 µm, and no coarse grain boundary phenomenon is inside.

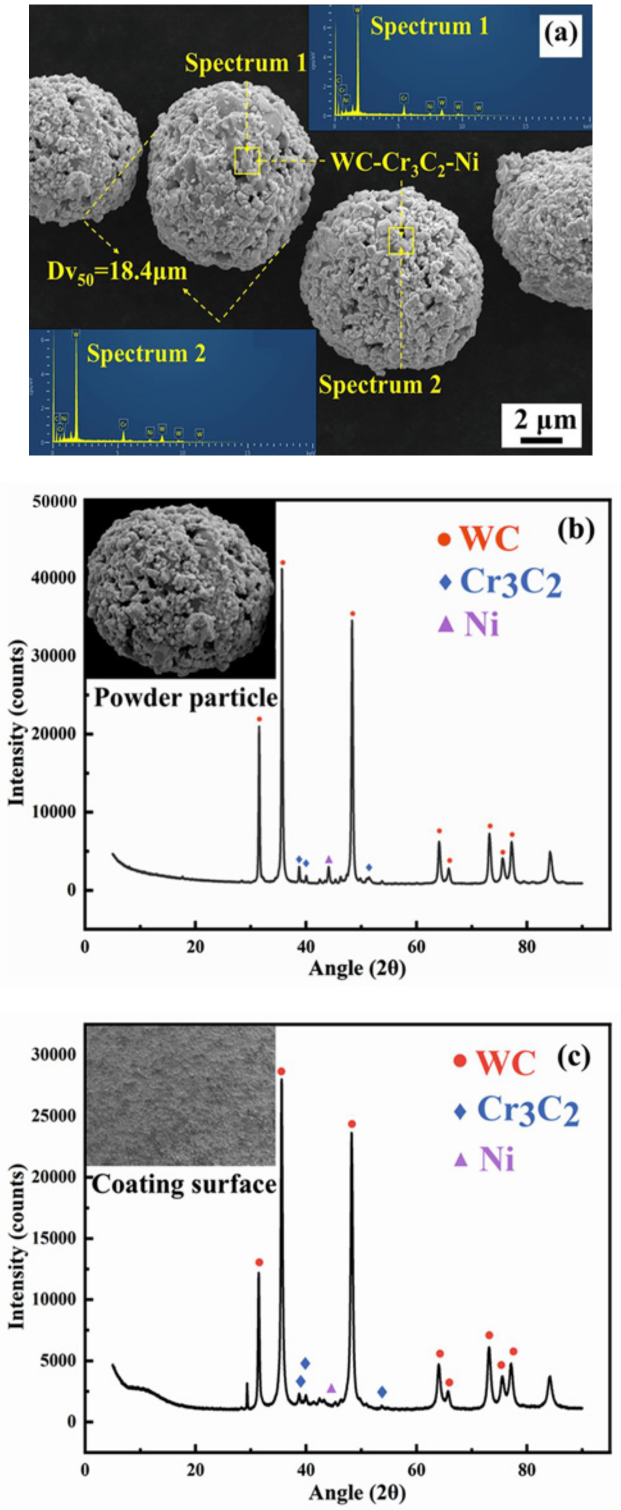

Fig. 2. (a) Particle morphology of WC-Cr_3C_2-Ni powder, (b) WC-Cr_3C_2-Ni powder phase analysis, and (c) WC-Cr_3C_2-Ni coating phase analysis.

As shown in Fig. 4a, the WC-Cr_3C_2-Ni coating on the semi-hard C17200 is compact and has no obvious defects, with a hardness exceeding 1200 HV0.5. After spraying, the coating thickness reached 281.17 (± 1.36) µm. The overall porosity was 0.34 %, well below the 3 % target in the thermal spray coating usage standard. The bonding mode between the coating and the substrate prepared by HVAF technology is mainly mechanical. Due to the extremely fast cooling rate of the coating droplet, it is difficult to form a large-scale metallurgical bonding between the two interfaces. The EDS test can find many Al-enriched corundum particles at the interface between the semi-

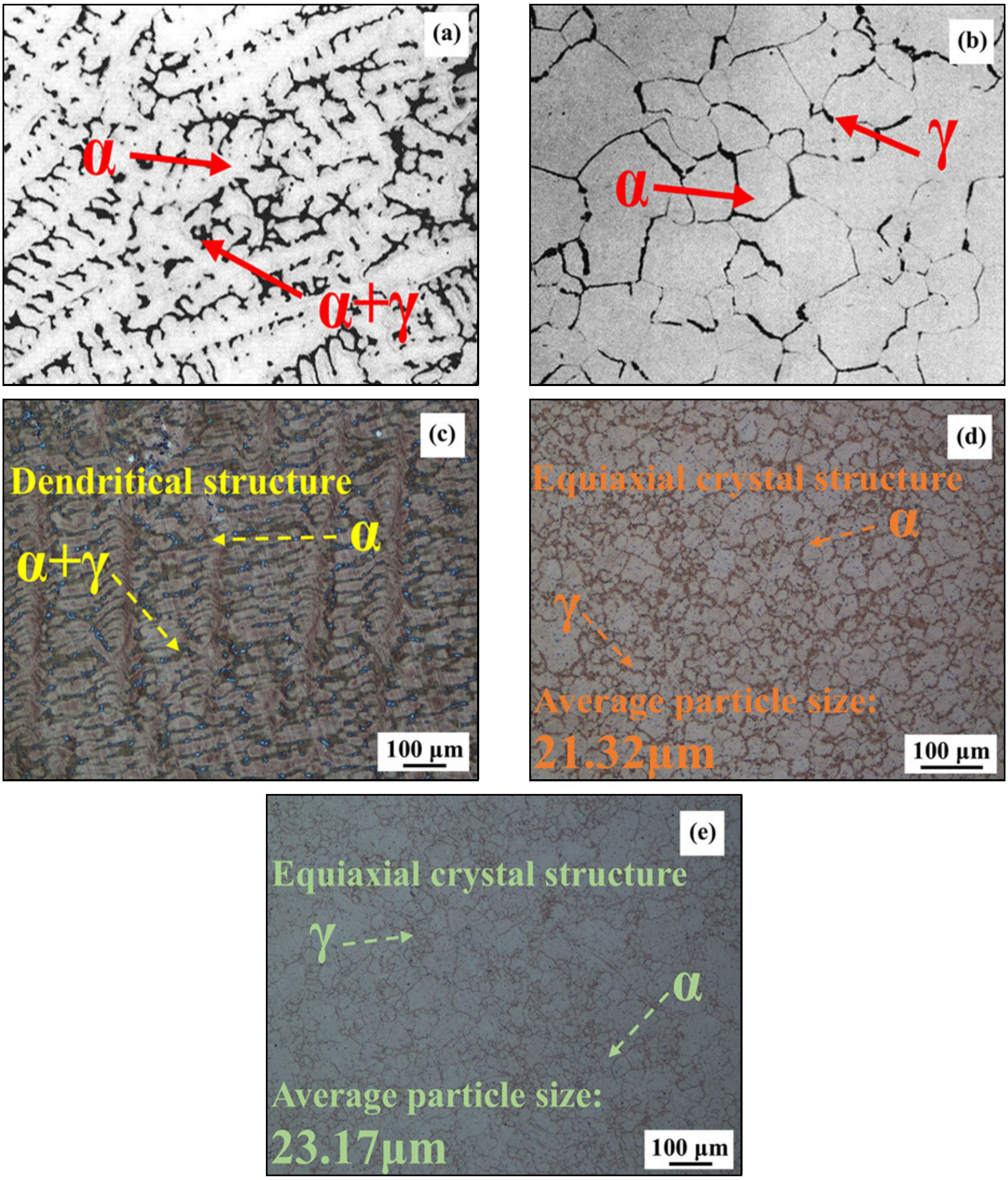

Fig. 3. (a) Semi-hard C17200 standard metallography, (b) full-hard C17200 standard metallography, (c) semi-hard C17200, (d) semi-hard C17200 after aging, and (e) full-hard C17200.

Table 1. HVAF spraying method of continuous casting crystallization roller

Processing method number	Substrate material	Heat treatment after HVAF	Design coating thickness (μm)
Method 1	Semi-hard C17200	–	300
Method 2	Semi-hard C17200	320 ℃, 2.5 h (Ar gas area)	300
Method 3	Full-hard C17200	–	300

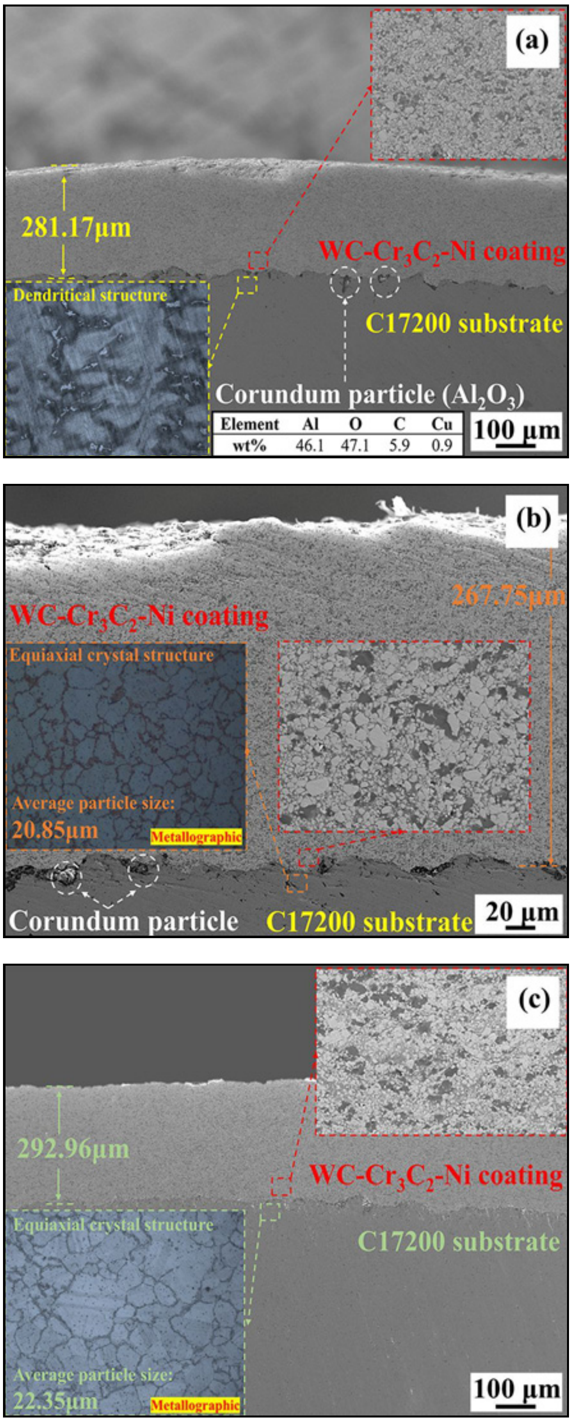

Element	Al	O	C	Cu
wt%	46.1	47.1	5.9	0.9

Fig. 4. Microstructure of WC-Cr_3C_2-Ni coating: (a) Method 1, (b) Method 2, and (c) Method 3.

hard C17200 and the coating. In Method 1, the internal crystal structure of the semi-hard C17200 roller body material is a dendrite structure. By observing the substrate structure of the binding site, it can be found that the dendrite structure of the site bombarded by liquid drops was not damaged or changed, which was consistent with the structure of the non-deposited substrate. As shown in Fig. 4b, after aging treatment, the internal structure of the sample substrate in Method 1 changes significantly from a dendrite structure to an equiaxial crystal structure, with a grain size of 20.85 μm. The grain size of the uncoated roller after aging treatment was 21.32 μm, which also indicated that the thermal shock during coating deposition did not have a significant effect on the microstructure of the substrate.

After aging treatment, the thermal conductivity increased from 66 to 105 $\mathrm{W\,m^{-1}\,K^{-1}}$, and the porosity of the WC-Cr_3C_2-Ni coating on its surface was 0.31 %. To explore the influence of the substrate structure on the spraying effect and analyze whether the surface grain of the substrate can be damaged during the spraying process, the roller body material was replaced with full-hard C17200 and sprayed again. As shown in Fig. 4c, in Method 3, the bonding interface between the coating and the substrate is smoother. After kinetic energy impact, the crystal structure of the roller surface was still stable, and the grain size was 22.35 μm. The substrate grains did not fracture or deform due to the impact, and there was no obvious change compared with the non-deposited original (grain size 23.17 μm). The extremely high hardness of the full-hard C17200 also avoided the embedding of corundum particles during sandblasting. At this point, the porosity of the WC-Cr_3C_2-Ni coating was 0.32 %. According to the changes of substrate and coating structure under the three processing methods, it can be found that the effect of carrying the WC-Cr_3C_2-Ni coating with full-hard C17200 was better.

3.2. Experimental analysis of thermal shock resistance of coatings

3.2.1. Thermal shock macroscopic failure of coatings

In the actual continuous casting process, the crystallization roller faces an extremely complex environment [27]. The roller surface is directly in contact with the liquid phase of the steel at 1600 ℃, and the flowing water inside carries the heat away. The long-term service environment puts forward clear requirements for the protective coating on the surface of the roller body, and the coating needs good thermal shock resistance. As shown in Fig. 5a, the coating prepared with Method 1 damages in the 17th cycle when facing the threat of thermal shock, and then completely fails in the 19th cycle. As shown in Fig. 5b, the first failure time of the Method 2 coating after aging treatment is delayed to the 19th cycle, and the complete failure life is extended to the 20th cycle. As shown in Fig. 5c, the complete failure life of the standard machined full-hard C17200 in Method 3 is increased to the 22nd cycle. The difference in thermal expan-

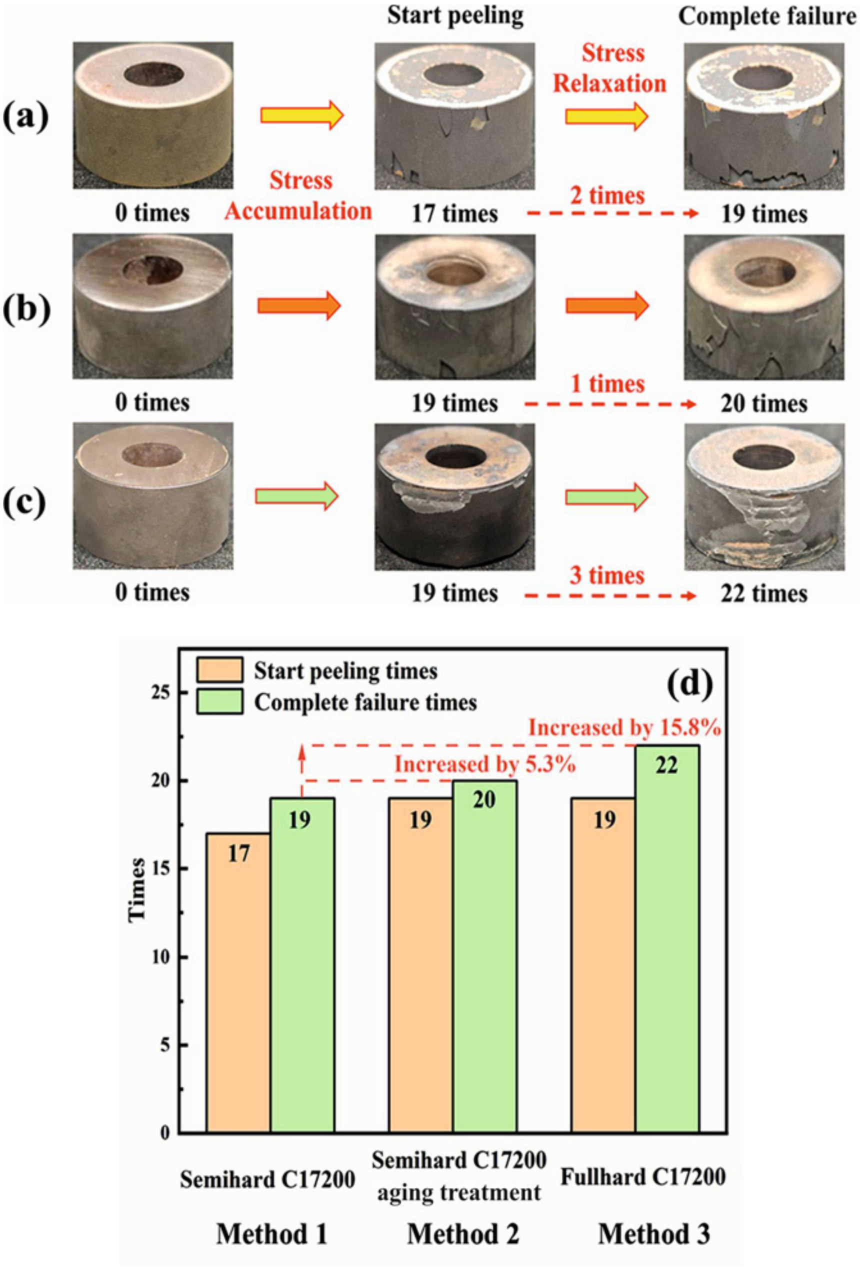

Fig. 5. (a) Thermal shock failure process of Method 1 roller sample, (b) thermal shock failure process of Method 2 roller sample, (c) thermal shock failure process of Method 3 roller sample, and (d) trend change of thermal shock resistance of roll body coating.

sion coefficient is the main reason for coating failure ($\mathrm{CTE}_{\mathrm{C17200}} = 17 \times 10^{-6}\,^{\circ}\mathrm{C}^{-1}$, $\mathrm{CTE}_{\mathrm{WC-Cr_3C_2-Ni}} = 7.3 \times 10^{-6}\,^{\circ}\mathrm{C}^{-1}$) [28]. As shown in Fig. 5d, processing methods 2 and 3 effectively increase the actual failure life by 5.3 and 15.8 %.

3.2.2. Microstructure of thermal shock failure zone of coatings

As shown in Fig. 6a, when the coating on the semi-hard C17200 surface is completely damaged, there are three characteristic regions at the failure site. The characteristic areas from bottom to top were the substrate, the substrate oxide layer, and the peeling coating, respectively. The existence of the flake oxide layer indicated that the failure crack originated in the semi-hard C17200 substrate first. This phenomenon allowed us to explain the complete failure process of the semi-hard C17200 surface coating. The thermal shock failure crack first occurred in the substrate, the coating carried part of the substrate away, and the substrate kept oxidizing with the coating and finally broke the coating. As shown in Fig. 6b, when semi-hard C17200 undergoes aging treatment, there are only two characteristic regions in the failure region. The initial thermal shock failure crack was transferred from the inner part of the substrate to the binding part of the substrate and coating, which also greatly reduced the volume loss of the surface substrate due to thermal shock. As shown in Fig. 6c, after replacing the base material of the roller with full-hard C17200, the failure region's failure process and morphology are the same as those of the sample in Method 2. The transformation of the crystal structure inhibited the initiation and expansion of thermal shock cracks inside the substrate, and the regular equiaxial crystal structure had a good effect on strengthening the internal stability of the substrate.

3.2.3. Phase analysis of coating thermal shock failure zone

As shown in Fig. 7a, the coating prepared by processing Method 1 carries a large amount of substrate at failure, so there are significant diffraction peaks of copper oxide (CuO, Cu_2O). The WC-Cr_3C_2-Ni coating also inevitably reacted in the face of extreme hot and cold alternating environments. The thermal shock reaction process was very complex, and the presence of Ni_3Cr_2, $NiWO_4$, and $NiCr_2O_4$ also proved that the actual service environment of the crystallization roller was harsh. As shown in Fig. 7b, the change of failure form in processing Method 2 leads to more substrate exposure on the surface of the roller body, which is reflected in the extremely obvious diffraction peaks of Cu and Cu oxides in the graph. The presence of $CuCrO_2$ also proved small-scale micro-zone metallurgical bonding between the substrate and the coating. As shown in Fig. 7c, when processing Method 3 is adopted, the final failure occurs inside the coating. Due to the accumulation of excessive residual stress in the coating, it quickly failed when slightly damaged [29]. This also explained why no obvious substrate oxide was found in the diffraction peak of thermal shock products on the surface of the roller body.

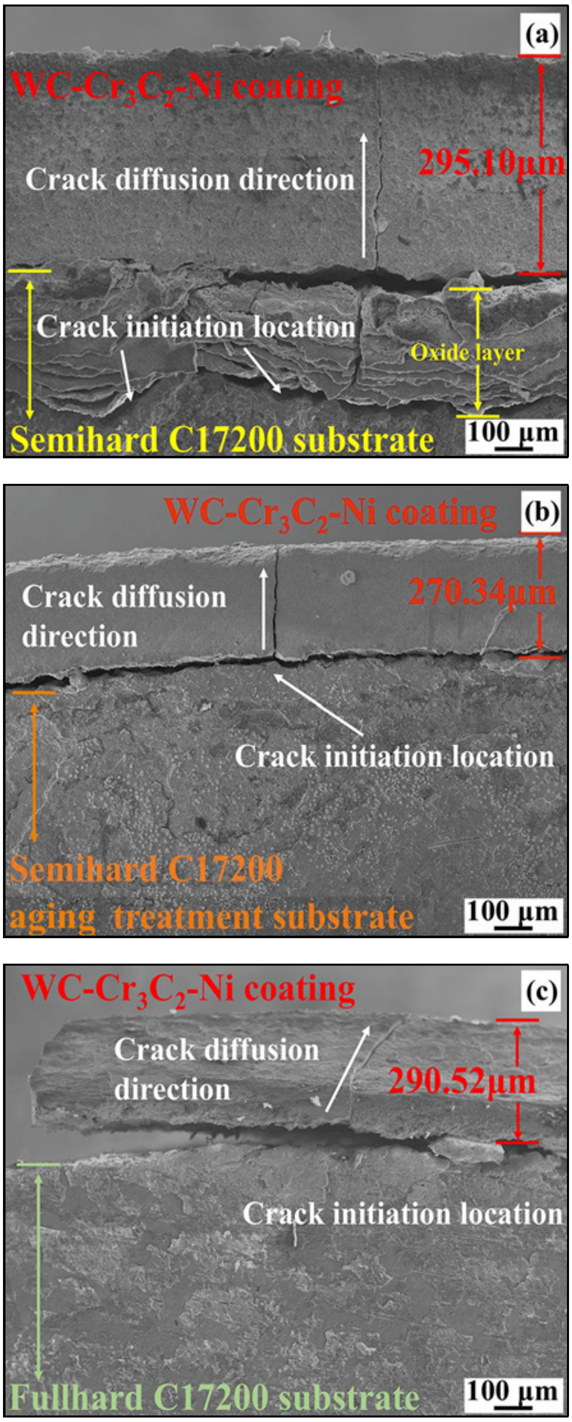

Fig. 6. Sample coating fracture section of (a) Method 1, (b) Method 2, and (c) Method 3.

3.2.4. Simplified fracture failure model of coating thermal shock failure

It is very important to determine the crack initiation location when studying the fracture of substrate surface coating. Many studies have suggested that the thermal stress inside the sample causes the failure of the coating. In this experiment, we simplified the complicated process of thermal stress to a simple tensile fracture model. In this model, the bonding strength between coating and substrate was an important factor affecting the failure mode. In industrial production, the binding force measurement of substrate surface coating has a detailed standard. However, this measurement standard is only for two-dimensional planar coatings and cannot describe the binding force of three-dimensional closed coatings in detail. In our simplified model, the binding condition of the substrate to the coating was considered the same everywhere. Therefore, we reduced the research scope of the thermal shock failure problem from the whole crystallization roller to a unit area at its bind-

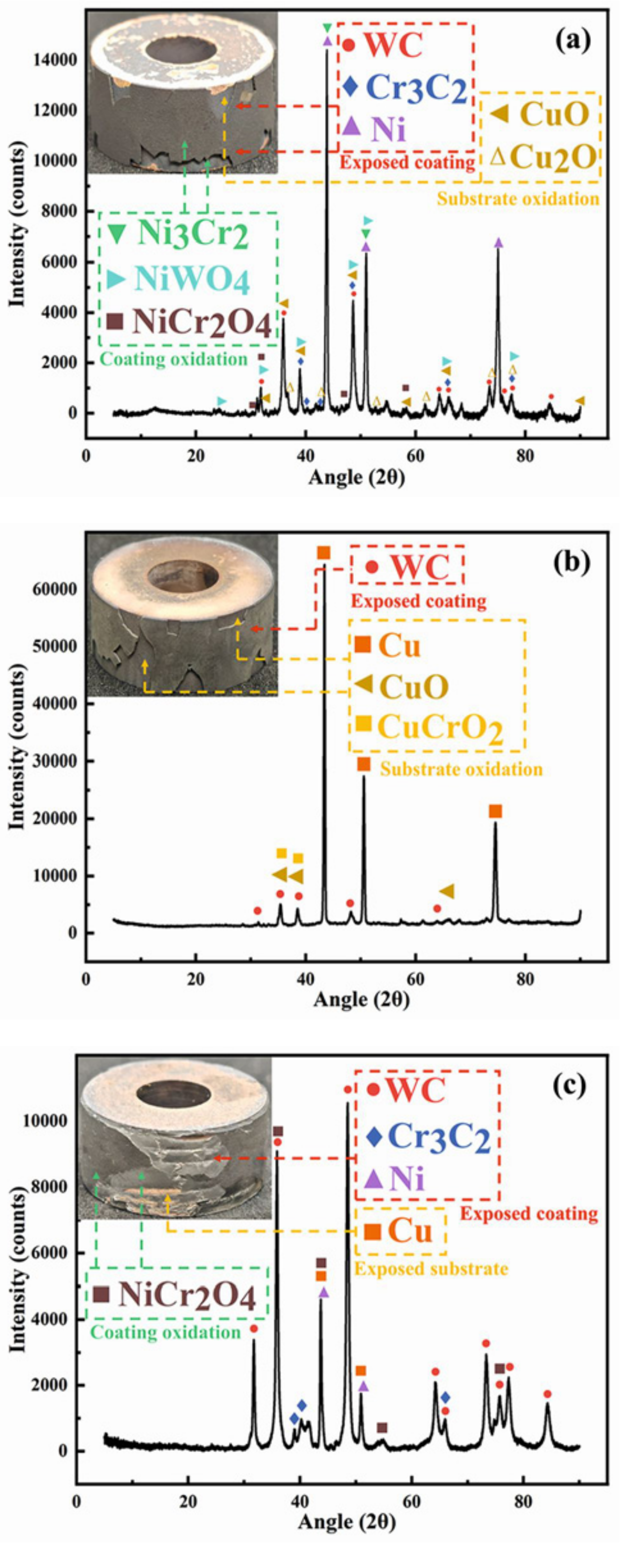

Fig. 7. Phase analysis of coating failure zone: (a) Method 1 sample, (b) Method 2 sample, and (c) Method 3 sample.

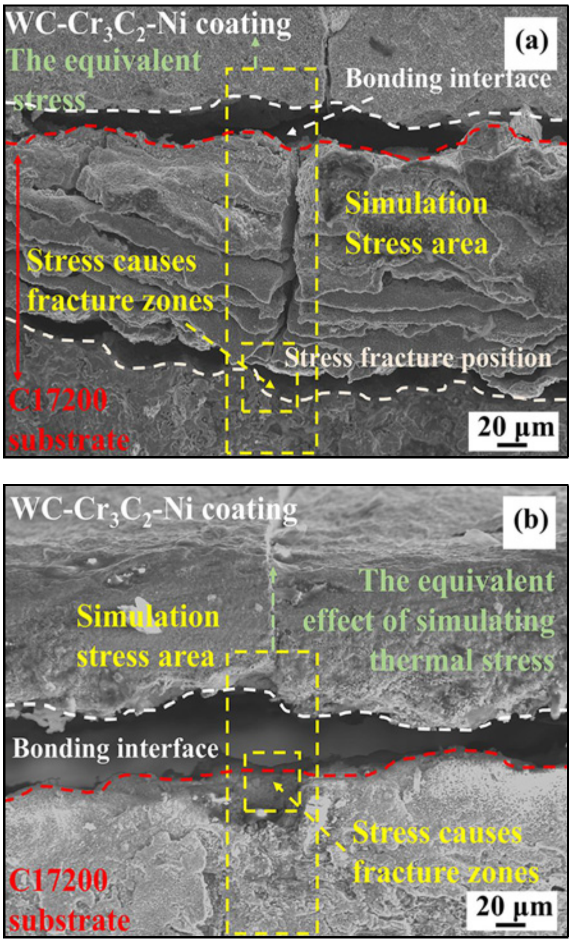

Fig. 8. (a) Low hardness substrate fracture form and (b) high hardness substrate fracture form.

ing interface. We equated the thermal stress in this region to a tensile force perpendicular to the bonding interface of the substrate coating. Since all the fracture behaviors occurred inside or on the surface of the substrate, a relationship was shown between the internal fracture failure of the sample and the tensile strength of the substrate. According to the Chinese industrial standard GB/T3362-2016 (hardness of metal materials and tensile strength conversion table), the tensile strength of semi-hard C17200 (220.72 HV0.5) and full-hard C17200 (430.26 HV0.5) is 705 and 1385 N mm^{-2}. As shown in Fig. 8a, the fracture first occurs inside the substrate when thermal stress affects the bonding area. This indicated that the bonding strength between the substrate and the coating was greater than the tensile strength of the substrate itself at this time. As shown in Fig. 8b, when the hardness of the substrate is increased, the fracture position of the sample occurs at the bonding area. The change of fracture position proved that the bonding strength of the substrate and coating was weaker than the tensile strength of full-hard C17200. The results showed that the coating-substrate bonding strength was between the tensile strength of the semi-hard and full-hard C17200. The above research proved that in-

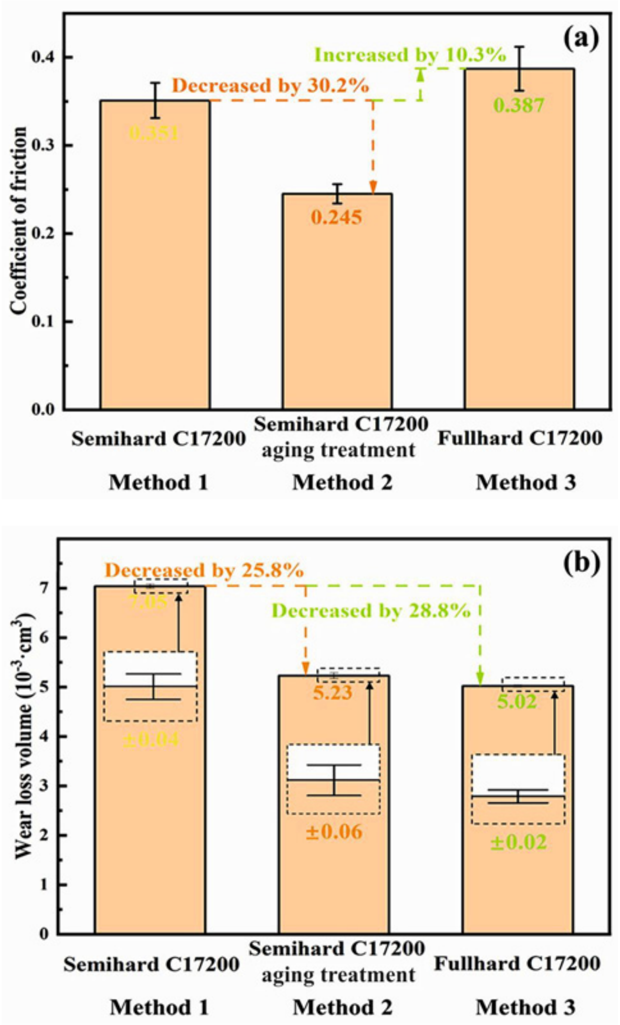

Fig. 9. (a) COF of each sample and (b) wear loss volume of each sample.

creased substrate hardness played a positive role in avoiding excessive substrate loss during thermal shock failure.

3.3. Reliability test of the rollers under 100 tons of steel equivalent wear condition

3.3.1. Coefficient of friction and wear loss volume analysis of crystallization rollers

Since the millimeter-level ultra-thin steel strip two-roll continuous casting production line was officially implemented in 2019, it can achieve a billet production speed of 3000 meters per hour (100 tons of steel). The wear resistance of the WC-Cr_3C_2-Ni coating deposited via HVAF technology was not affected by the change of the base material, and the temperature of the substrate aging treatment did not cause an oxidation threat to the coating. In this experiment, we focused more on the high-temperature wear resistance of the exposed substrate once the coating fell off the surface of the roller body. We used samples with a diameter of 40 mm under a high temperature and load environment, with a rotation wear of 12,500 turns, and a total wear distance of more than 3000 meters. The wear condition equivalent to that of 100 tons of steel produced under actual working conditions was set to analyze the service reliability of the roller after the coating fell off. As shown in Fig. 9a, semi-hard C17200 treated with Method 2 reduces the COF (coefficient of friction) on the surface of the roller body from 0.351 to 0.245. On the contrary, the COF of the roller body surface increased due to the commercial full-hard C17200 in Method 3. In long-term studies, although the COF is an important parameter to characterize the change of wear resistance of materials, it is not a decisive factor. As shown in Fig. 9b, the substrate in Method 2 and Method 3 both play a role in reducing the volume of roller surface wear loss from 7.05×10^{-3} to $5.23 \times 10^{-3}\ \mathrm{cm}^3$ (25.8 % lower) and $5.02 \times 10^{-3}\ \mathrm{cm}^3$ (28.8 % lower), respectively. The full-hard C17200 in Method 3 showed the best wear resistance and service stability. The experimental results showed that either the self-aging treatment or the direct replacement of the base material can improve the stability of the crystallization roller when facing the risk of coating failure.

3.3.2. Microstructure of wear area of crystallization roller

In the long-term production practice, the researchers found that the wear failure of the material surface was not only caused by a single wear mechanism. The crystallization roller also suffered wear failure under the action of various mechanisms. At the initial stage of the wear process, the surface of the roller came into contact with the cooled billet under the action of high-load extrusion. The contact point of the two interfaces was sticky, and the shear force during the rotation of the roller caused the bonding substrate to break away from the surface, and the wear process at this time was also considered adhesive wear [30]. When the integrity of the exposed area of the roller was damaged, the debris that could not break away from the wear interface caused secondary damage to the substrate, leaving clear plowings, which were also considered abrasive wear [31]. Under normal circumstances, the continuous casting production line ran continuously to ensure production. The fatigue wear occurred when the surface of the roller body was subjected to cyclic stress during long-term service [32]. Oxidative wear accompanied by a high-temperature environment caused the exposed substrate of the roller body to form brittle oxide and fall off [33]. As shown in Figs. 10a–c, the combined actions of multiple wear

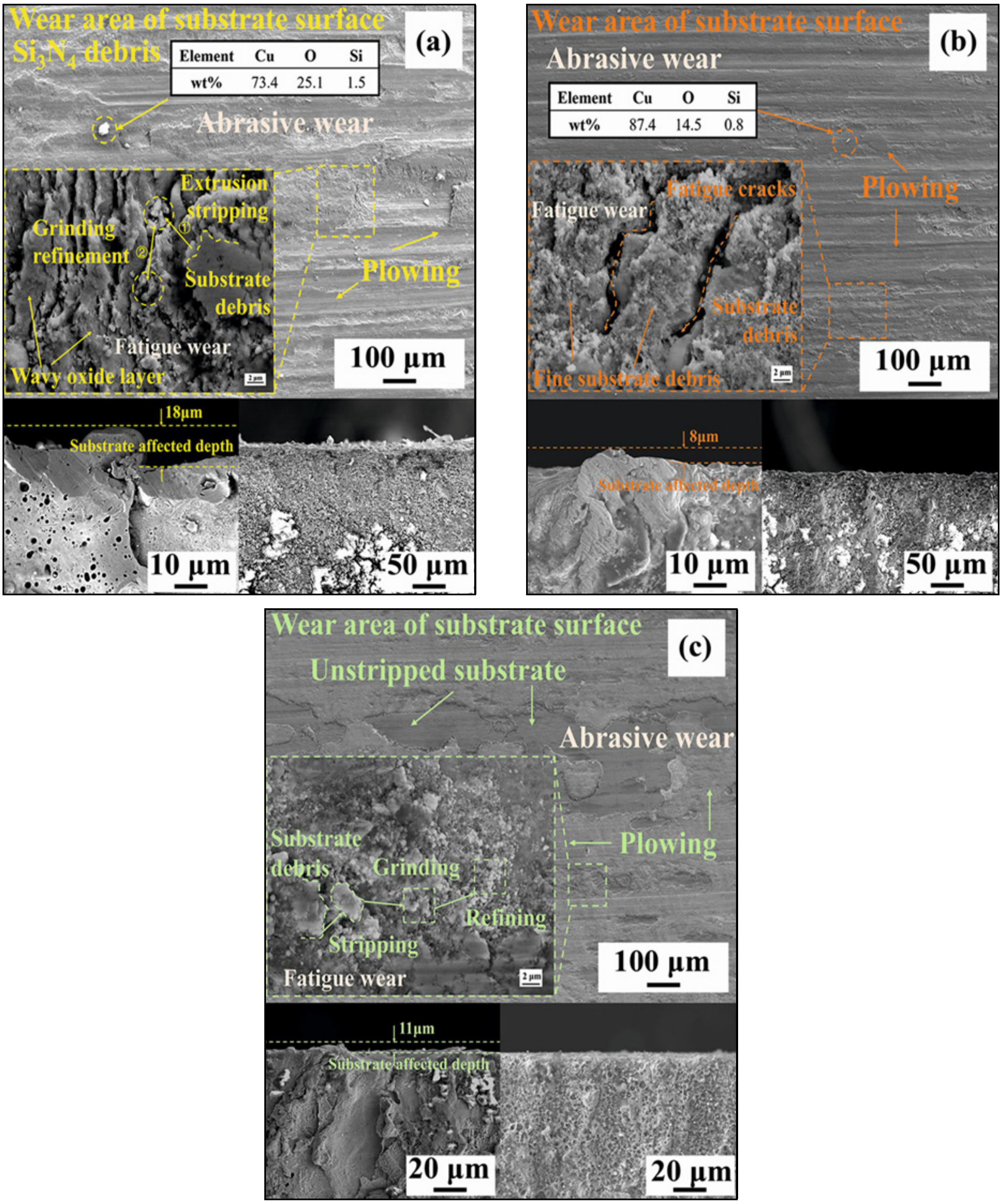

Element	Cu	O	Si
wt%	73.4	25.1	1.5

Element	Cu	O	Si
wt%	87.4	14.5	0.8

Fig. 10. The morphology of the wear area and the depth of surface affected by wear: (a) Method 1 sample, (b) Method 2 sample, and (c) Method 3 sample.

mechanisms are found on the surface of each substrate material. It can be found that the substrate materials in Methods 2 and 3 effectively reduced the affected depth of the roller body surface from 18 to 8 μm and 11 μm, respectively. At the same time, the substrate also showed good bearing capacity for the WC-Cr_3C_2-Ni coating, and the coating wear area in each method was too small to measure the affected depth. In summary, it can be seen that Methods 2 and 3 played a good role in improving the wear resistance performance of the roller body.

3.4. Production cost calculation of each processing method

When we explored the effect of processing methods

Table 2. Crystallization roller size parameters

Sample	Material	Length (mm)	Diameter (mm)
Crystallization roller	Semi-hard C17200	1700	850

Table 3. The cost of preparing a crystallization roller by each processing method

	Method 1	Method 2	Method 3
Cost (Thousand dollar)	276	277	315
Cost changes (Increased by)	–	0.4 %	14.1 %

on coating and substrate properties, processing and production costs must be considered. The cost of the crystallization roller in the two-roll continuous casting process is very expensive, so the innovation of the process must be based on cost calculation. In actual production, the C17200 bar is machined into a sleeve shape and installed on a high-hardness stainless steel shaft by interference nesting. Therefore, in measuring the cost, we considered the purchase of raw materials, the cost of heat treatment, and the difficulty of processing. The specific parameters of the crystallization rollers in our continuous casting production line are shown in Table 2.

The raw material volume of C17200 was 9.64×10^5 cm^3, and the density of C17200 was 8.3 g cm^{-3}. According to the volume calculation Eq. (1):

$$\rho = \frac{M}{V}, \quad (1)$$

where ρ is the density of the material in g cm^{-3}, M is the mass of the material in g, V is the volume of the material in cm^3. Finally, the raw material mass of the crystallization roller was 8×10^3 kg. Raw material supplier quotation: semi-hard C17200 price is \$ 34.5/kg, and full-hard C17200 price is \$ 39.4/kg. The factory used argon atmosphere vacuum heat treatment industrial furnace energy consumption of 60 kWh, considering the gas use and component loss, the operating cost was not more than \$ 500 per hour. The cost after comprehensive calculation is shown in Table 3.

According to the calculation, the theoretical cost of Method 2 and Method 3 was 0.4 and 4.1 % higher than the existing process. At the same time, we found that ordinary stainless steel drill bits were difficult to process full-hard C17200 in the turning process. Combined with the reliability study of each processing method mentioned above, the self-aging treatment of semi-hard C17200 after spraying can obtain the performance of commercial full-hard C17200 and avoid the difficulties caused by reprocessing. More importantly, Method 2 had the lowest cost increase and the best economic benefit.

4. Conclusions

In this experiment, we improved the processing method of the crystallization roller and deposited the WC-Cr$_3$C$_2$-Ni coating on its surface. The semi-hard C17200 roller used in the production line has demonstrated excellent coating bearing and harsh environment service performance. After spraying, the WC-Cr$_3$C$_2$-Ni coating on the roller body showed a good state, with high hardness (more than 1200 HV0.5). Increasing and adjusting the processing sequence positively improved the performance of crystallization rollers, including theoretical research and practical production.

(1) Theoretical research: In the thermal shock test and wear test, the aging treatment standard and its change in the process flow did not affect the improvement of crystallization roller performance. The hardness of C17200 after heat treatment increased from 220.72 to 430.26 HV0.5, and the thermal shock life of the surface coating increased from 19 times to 20 times. The hardness of C17200 after standard heat treatment and spraying was also above 420 HV0.5, and the thermal shock life of its surface coating was further increased to 22 times. The C17200 showed stronger wear resistance regardless of the self or the commercial standard aging treatment process in the experiment simulating the coating failure and the roller body being threatened by wear.

(2) Actual production: The raw crystallization roller base material cost \$ 276 thousand, and the total cost of using the self-aging treatment process increased to \$ 277 thousand (0.4 % increase). For the replacement of industry-standard production of the same material, the total cost increased to \$ 315 thousand (14.1 % increase). The change in economic cost proved that self-aging treatment had the most practical application prospect, and the cost reduction and efficiency increase were obvious.

Acknowledgements

The authors would like to express their gratitude for the financial support from the National Natural Science Foundation of China (Grant No. 52174302, 51932008), the Science and Technology Program of Liaoning of China (2023JH2/101700304).

References

[1] L. Dong, H. Zhang, T. Fujita, S. Ohnishi, H. Q. Li, M. Fujii, H. J. Dong, Environmental and economic gains of industrial symbiosis for Chinese iron/steel industry: Kawasaki's experience and practice in Liuzhou and Jinan, J. Clean. Prod. 59 (2013) 226–238. https://doi.org/10.1016/j.jclepro.2013.06.048

[2] L. Y. Yan, A. J. Wang, Based on material flow analysis: Value chain analysis of China iron resources, Resour. Conserv. Recycl. 91 (2014) 52–61. https://doi.org/10.1016/j.resconrec.2014.07.010

[3] Y. X. Liu, H. J. Li, S. P. Huang, H. Z. An, R. Santagata, S. Ulgiati, Environmental and economic-related impact assessment of iron and steel production. A call for shared responsibility in global trade, J. Clean. Prod. 269 (2020) 122239. https://doi.org/10.1016/j.jclepro.2020.122239

[4] H. G. Zhong, R. J. Wang, Q. Y. Han, M. T. Fang, H. Z. Yuan, L. X. Song, X. Xie, Q. J. Zhai, Solidification structure and central segregation of 6Cr13Mo stainless steel under simulated continuous casting conditions, J. Mater. Res. Technol. 20 (2022) 3408–3419. https://doi.org/10.1016/j.jmrt.2022.08.115

[5] S. K. Vil'danov, L. V. Rogaleva, P. I. Chernousov, A. E. Karpalev, V. O. Podusovsky, Evaluating the effects of certain process parameters on the metal cooling rate in a steel ladle, Metall. 66 (2022) 518–524. https://doi.org/10.1007/s11015-022-01355-6

[6] R. Zhang, H. B. Li, H. C. Zhu, Z. H. Jiang, H. Feng, S. C. Zhang, Cooling capacity evolution of steel strip during oscillatory feeding process in slab continuous casting, Steel. Res. Int. 95 (2023) 2300252. https://doi.org/10.1002/srin.202300252

[7] C. Misirli, M. Ceviz, I. Çetintav, H. Kiliç, Effect of high temperatures on dry sliding friction and wear behaviour of CuCrZr copper alloy, Mater. Test. 65 (2023) 258–266. https://doi.org/10.1515/mt-2022-0270

[8] D. M. Liu, Z. L. Xue, S. Q. Song, Effect of cooling rate on non-metallic inclusion formation and precipitation and micro-segregation of Mn and Al in Fe-23Mn-10Al--0.7C steel, J. Mater. Res. Technol. 24 (2023) 4967–4979. https://doi.org/10.1016/j.jmrt.2023.04.024

[9] L. Li, F. S. Du, Effects of sinusoidal vibration of crystallization roller on composite microstructure of Ti/Al laminated composites by twin-roll casting, J. Wuhan. Univers. Technol.-Mater. Sci. Edit. 39 (2024) 196–205. https://doi.org/10.1007/s11595-024-2872-z

[10] L. Li, F. S. Du, Effects of sinusoidal vibration of crystallization roller on microstructure and mechanical properties of Ti/Al laminated composites by twin-roll casting, Trans. Indian. Inst. Met. 76 (2023) 2073–2083. https://doi.org/10.1007/s12666-022-02795-z

[11] Y. W. Wu, Z. Q. Rao, X. C. Chen, R. Wang, H. B. Bai, Mechanics behaviors and electrical conductivity of beryllium bronze alloy entangled metallic wire material: Experimental study and theoretical modeling, J. Mater. Res. Technol. 29 (2024) 728–737. https://doi.org/10.1016/j.jmrt.2024.01.126

[12] N. V. Semenchuk, A. V. Kolubaev, O. V. Sizova, Y. A. Denisova, A. A. Leonov, Structure and properties of multilayer CrN/TiN coatings obtained by vacuum-arc plasma-assisted deposition on copper and beryllium bronze, Russ. Phys. J. 66 (2023) 1077–1086. https://doi.org/10.1007/s11182-023-03045-5

[13] I. Lomakin, A. Nigmatullina, X. Sauvage, Nanostructuring of beryllium bronze: Contribution of grain boundaries segregation and solid solution, Mater. Lett. 357 (2024) 135632. https://doi.org/10.1016/j.matlet.2023.135632

[14] Z. Y. Zhang, W. Z. Li, R. X. Yang, X. L. Zhao, H. A. Zhang, Microstructure and tribo-behavior of WC-Cr_3C_2-Ni coatings by laser cladding and HVAF sprayed: A comparative assessment, Mater. 16 (2023) 2269. https://doi.org/10.3390/ma16062269

[15] E. Jonda, L. Łatka, M. Godzierz, A. Maciej, Investigations of microstructure and corrosion resistance of WC-Co and WC-Cr_3C_2-Ni coatings deposited by HVOF on magnesium alloy substrates, Surf. Coat. Technol. 459 (2023) 129355. https://doi.org/10.1016/j.surfcoat.2023.129355

[16] E. Jonda, L. Łatka, M. Godzierz, K. Olszowska, A. Tomiczek, Microstructure, residual stress and mechanical properties of double carbides cermet coatings manufactured on AZ31 substrate by high velocity oxy-fuel spraying, Arch. Civil. Mech. Eng. 24 (2024) 61. https://doi.org/10.1007/s43452-024-00867-z

[17] R. Gao, Y. F. Huang, X. Y. Zhou, G. Z. Ma, G. Jin, T. H. Li, H. D. Wang, M. Liu, Material system and tribological mechanism of plasma sprayed wear resistant coatings: Overview, Surf. Coat. Technol. 483 (2024) 130758. https://doi.org/10.1016/j.surfcoat.2024.130758

[18] O. Prakash, R. Chandrakar, L. Martin, J. Verma, A. Kumar, A. Jaiswal, Laser cladding technology for high entropy alloys: Effect and applications, Mater. Res. Expr. 11 (2024) 096510. https://doi.org/10.1088/2053-1591/ad75e8

[19] X. Liu, C. L. Shen, K. Hu, S. H. Zhang, Z. L. Xue, Y. Yang, Improvement in high-velocity air-fuel-sprayed Cr_3C_2-NiCr/(NiAl, NiCr) composite coatings by annealing heat treatment, J. Mater. Eng. Perform. 32 (2023) 199–210. https://doi.org/10.1007/s11665-022-06938-7

[20] K. Torkashvand, S. Joshi, M. Gupta, Advances in thermally sprayed WC-based wear-resistant coatings: Co-free binders, processing routes and tribological behavior, J. Therm. Spray. Technol. 31 (2022) 342–377. https://doi.org/10.1007/s11666-022-01358-4

[21] L. Ding, H. X. Wang, X. M. Quan, Effect of aging treatment on microstructure and wear properties of CoCrFeNiTiNbB1.25 high entropy alloys coatings by laser cladding, Sci. Adv. Mater. 13 (2021) 1280–1288. https://doi.org/10.1166/sam.2021.4057

[22] S. Qu, X. W. Sun, Z. X. Dong, Y. Liu, H. R. Yang, W. F. Zhang, S. B. Mu, Z. X. Wang, T. B. Yu, J. Zhao, Simulation and experimental investigation of material removal profile based on ultrasonic vibration polishing of K9 optical glass, Tribol. Int. 196 (2024) 109730. https://doi.org/10.1016/j.triboint.2024.109730

[23] R. J. Alroy, R. Pandey, M. Kamaraj, G. Sivakumar, Role of process parameters on microstructure, mechanical properties and erosion performance of HVAF sprayed Cr_3C_2-NiCr coatings, Surf. Coat. Technol. 449

(2022) 128941.
https://doi.org/10.1016/j.surfcoat.2022.128941

[24] S. L. Liu, X. P. Zheng, G. Q. Geng, Influence of nano-WC-12Co powder addition in WC-10Co-4Cr AC-HVAF sprayed coatings on wear and erosion behaviour, Wear 269 (2010) 362–367.
https://doi.org/10.1016/j.wear.2010.04.019

[25] R. J. Alroy, M. Kamaraj, D. V. Lakshmi, K. Praveen, P. S. Babu, G. Sivakumar, Tailoring microstructural features of Cr_3C_2-25NiCr coatings through diverse spray variants and understanding the high-temperature erosion behavior, Tribol. Int. 188 (2023) 108810.
https://doi.org/10.1016/j.triboint.2023.108810

[26] G. L. Xie, Q. S. Wang, X. J. Mi, B. Q. Xiong, L. J. Peng, The precipitation behavior and strengthening of a Cu-2.0 wt.% Be alloy, Mater. Sci. Eng. A-Struct. Mater. Prop. Microstruct. Process. 558 (2012) 326–330. https://doi.org/10.1016/j.msea.2012.08.007

[27] B. Qiang, X. Liu, H. Wu, J. Wu, H.C. Shi, Y. D. Li, Experimental investigation on elevated temperature mechanical properties in cast steel joints, Struct. 62 (2024) 106158.
https://doi.org/10.1016/j.istruc.2024.106158

[28] Z. Sun, S. G. Zhu, W. W. Dong, Y. F. Bai, H. Ding, Y. L. Luo, P. Di, Characteristic comparison of stacked WC-based coatings prepared by high-velocity oxygen-fuel spray and electric contact strengthening, Surf. Coat. Technol. 421 (2021) 127289.
https://doi.org/10.1016/j.surfcoat.2021.127289

[29] W. J. He, T. Shioya, Conditions of micro-cracking and their applications to ceramic coatings of carbon-carbon composites, Compos. Part A-Appl. Sci. Manuf. 28 (1997) 689–694.
https://doi.org/10.1016/S1359-835X(97)00023-7

[30] C. Zhang, J. Zhang, R. Hu, M. Zhang, Y. W. Zhang, W. H. Wu, G. S. Li, X. G. Lu, Heat treatment-induced wear transition in electroplated Ni-Co coating on copper, Adv. Eng. Mater. 24 (2022) 2200402.
https://doi.org/10.1002/adem.202200402

[31] D. Yonekura, J. Fujita, K. Miki, Fatigue and wear properties of Ti-6Al-4V alloy with Cr/CrN multilayer coating, Surf. Coat. Technol. 275 (2015) 232–238.
https://doi.org/10.1016/j.surfcoat.2015.05.014

[32] C. Guo, J. S. Zhou, J. R. Zhao, L. Q. Wang, Y. J. Yu, J. M. Chen, H. D. Zhou, Microstructure and tribological properties of a HfB2-containing Ni-based composite coating produced on a pure Ti substrate by laser cladding, Tribol. Lett. 44 (2011) 187–200.
https://doi.org/10.1007/s11249-011-9837-z

[33] Z. Geng, S. H. Hou, G. L. Shi, D. L. Duan, S. Li, Tribological behaviour at various temperatures of WC-Co coatings prepared using different thermal spraying techniques, Tribol. Int. 104 (2016) 36–44.
https://doi.org/10.1016/j.triboint.2016.08.025